RSC Advances

PAPER

View Article Online
View Journal | View Issue

Cite this: *RSC Adv.*, 2017, **7**, 13406

Nitrogen doped graphite felt decorated with porous $Ni_{1.4}Co_{1.6}S_4$ nanosheets for 3D pseudocapacitor electrodes†

Xiang Zhang, Yuying Zheng,* Jun Zhou, Wenqing Zheng and Dongyang Chen*

Received 12th December 2016
Accepted 21st February 2017

DOI: 10.1039/c6ra28083h

rsc.li/rsc-advances

3D electrodes are of significant importance for the development of wearable electronics. In this manuscript, nitrogen doped graphite felt (NGF) and $Ni_{1.4}Co_{1.6}S_4$ have been selected as a 3D conducting matrix and redox-active species for pseudocapacitor electrodes, respectively. The hydrothermal growth of $Ni_{1.4}Co_{1.6}S_4$ in the presence of NGF yields stand-alone and bendable composite electrodes where $Ni_{1.4}Co_{1.6}S_4$ forms porous nanosheets dispersed uniformly along the NGF surface. The experimental results show that the $Ni_{1.4}Co_{1.6}S_4$/NGF electrode achieves a remarkable specific capacitance of 1625 F g^{-1} at a current density of 1 A g^{-1}, which is maintained at 1465 F g^{-1} when the current density is increased to 20 A g^{-1}. After cycling at a current density of 20 A g^{-1} for 2000 cycles, the $Ni_{1.4}Co_{1.6}S_4$/NGF electrode still delivers 90.2% of its original specific capacitance. Such encouraging rate capability and cycling stability of the $Ni_{1.4}Co_{1.6}S_4$/NGF electrode are attributed to the desirable $Ni_{1.4}Co_{1.6}S_4$ nanostructure and the synergistic effect of the good electron conductivity and excellent surface property of the NGF substrate. The outstanding electrochemical performance of the $Ni_{1.4}Co_{1.6}S_4$/NGF electrode makes it a promising candidate for 3D pseudocapacitor applications.

1. Introduction

The current global concerns over energy have galvanized a lot of efforts to develop innovative energy storage technologies with high energy efficiency, improved power density and considerable sustainability. Supercapacitors are one of the many types of energy storage technologies that hold the prospect to address these concerns.[1,2] Two categories of supercapacitor have been reported so far, namely electrostatic double-layer capacitors (EDLCs) and pseudocapacitors. The EDLC is intrinsically limited by its specific energy density, therefore, many works have focused on pseudocapacitor development. Consisting of redox-active species and carbon substrates, pseudocapacitors usually feature higher power density than batteries yet higher energy density than EDLCs.[3,4] However, the strategy to design pseudocapacitor electrodes for devices to satisfy the performance metrics for practical applications such as portable devices and hybrid electric vehicles is still an ongoing research challenge.[5]

Various carbon substrates have been proposed for high performance pseudocapacitor electrodes, such as graphene,[4] carbon nanotubes,[6] mesoporous carbon,[7] heteroatom-doped carbon,[8–10] *etc.* The key properties for carbon substrates include large specific surface area, good wettability, high electron conductivity, and robust mechanical strength. Among the carbon substrates reported so far, graphite felt (GF) with considerable pore volume as well as anti-deformation characteristics has been regarded as a promising candidate for pseudocapacitors.[11] Featuring stable 3D structures, GF is capable to avoid the agglomeration of active materials, afford a short diffusion length for ions and a smooth pathway for electrons.[12] To overcome the property of poor capacitance, which is a general drawback of most carbon materials, many approaches have been performed on GF internally or externally, such as nitrogen modification or sulfide decoration. For example, He *et al.*[13] reported that the N-doped GF exhibits a discharge capacity of 79.2 mA h, much higher than that of the untreated GF. Jeong *et al.*[14] blended GF with nitrogen-doped CNTs and also achieved improved electrochemical performance.

Integrating transition metal sulfides such as NiS,[15] CoS_2,[16] and $NiCo_2S_4$ (ref. 17) onto carbon substrates has been proven to be an effective way to significantly increase the specific capacitance of pseudocapacitors. Particularly, $NiCo_2S_4$, which possesses the electrochemical contribution from both nickel and cobalt ions,[18] exhibits faster electron transfer and better redox capability compared with the corresponding single component sulfides.[19,20] Rivaling to the $NiCo_2O_4$,[21] $NiCo_2S_4$ can well maintain the structure with expanded interlayer spacing during charge/discharge process, owing to the lower electronegativity of sulfur than that of oxygen.[22] Additionally, the shape

College of Materials Science and Engineering, Fuzhou University, Fuzhou 350116, P. R. China. E-mail: yyzheng@fzu.edu.cn; dongyang.chen@fzu.edu.cn; Fax: +86 591 22866524; Tel: +86 591 22866524

† Electronic supplementary information (ESI) available. See DOI: 10.1039/c6ra28083h

of $NiCo_2S_4$ can be easily controlled under certain reaction condition to form sheet, burl or tube-like $NiCo_2S_4$.[17,21,23] For instance, Peng *et al.*[17] reported a facile hydrothermal method for the growth of sheet-like $NiCo_2S_4$ on graphene, which present a specific capacitance of 1161 F g^{-1} at 5 A g^{-1} and maintained a high value of 1108 F g^{-1} after 2000 cycles. Sun *et al.*[23] prepared a type of burl-like $NiCo_2S_4$ on carbon fiber paper/cloth, achieving a specific capacitance of 0.83 F cm^{-2} at a high current density of 25 mA cm^{-2} and a capacitance retention of 75.9% after 5000 cycles. Those results also infer that the combination of conductive carbon substrate and pseudocapacitive $NiCo_2S_4$ may individualize the pseudocapacitors with prominent cycling performance while retaining the high capacitance of $NiCo_2S_4$.

In our previous work,[24] we have reported a method for synthesizing polyaniline-grafted graphene, which exhibited a preferable pseudocapacitive performance. To increase the specific capacitance of pseudocapacitors as well as ensure flexibility for applications in wearable electronics, herein, we report the preparation of stand-alone pseudocapacitor electrodes with N-doped graphite felt (NGF) as 3D matrix and $Ni_{1.4}Co_{1.6}S_4$ nanosheets hydrothermally grown on NGF as redox-active species. In such design, rigid nickel form substrate is replaced by bendable NGF, and poor adhesion between active material and the substrate is resolved. The NGF was prepared by an *in situ* polymerization of polyaniline (PANI) on the GF surface followed by pyrolyzing under N_2 atmosphere at high temperature to induce the N–C exchange between PANI and the GF. After that, a two-step hydrothermal method was adopted to deposit $Ni_{1.4}Co_{1.6}S_4$ onto the GF surface, including the prior *in situ* growth of NiCo-precursors and the following S^{2-}-induced corrosion process. The structure and electrochemical performance of the as-prepared electrodes were fully characterized and closely correlated.

2. Experimental

2.1 Material

Natural graphite felt (99.7%, 500 mesh) was supplied by Boshengtianhong New Materials Technology Company (Changsha, China). All other reagents were purchased from Sinopharm Chemical Reagent Company (Shanghai, China). Aniline was distilled twice under reduced pressure and other reagents were used as received without further treatment.

2.2 Preparation of N-doped graphite felt (NGF)

The NGF was prepared according to the following method. A piece of GF (2 cm × 2 cm) was treated with ethanol, diluted hydrochloric acid and sodium hydroxide in an ultrasound bath, and then washed with deionized water for several times until pH is neutral. After drying under vacuum at 80 °C overnight, the GF was immersed in 80 mL of aniline solution (varying concentrations) and hydrochloric acid solution (1 M). Afterwards, 20 mL of hydrochloric acid (1 M) containing 150 mg of ammonium persulfate (APS) was added slowly into the reaction system and ultrasonically polymerized at 25 °C for 1 h. Finally, the resultant GF was pyrolyzed under N_2 atmosphere at one of the three different temperatures (800, 900, and 1000 °C) for 1 h. The samples were described as NGF-*x*-*y*, where *x* is the concentration of aniline used in the reaction, and *y* is the pyrolysis temperature.

2.3 Growth of NiCo-sulfides on NGF

0.1 g of NGF was treated with concentrated nitric acid at 80 °C for 2 h and washed with deionized water until pH is neutral. Then, the acidic NGF was put into a 30 mL of mixed solution of ethanol and deionized water (volume ratio = 1 : 1), which contains 0.36 g of urea, 0.35 g of hexamethylenetetramine (HMT), 0.407 g $Ni(NO_3)_2 \cdot 6H_2O$ and 0.466 g $Co(NO_3)_2 \cdot 6H_2O$. After ultrasonic dispersing for 3 h, the mixture was transferred into a 50 mL Teflon-lined stainless steel autoclave, and heated at 100 °C for 6 h to form NiCo-precursors. After being cooled down to room temperature, the NiCo-precursors/NGF was washed with deionized water and lyophilized overnight. Afterwards, the obtained NiCo-precursors/NGF was added into a 50 mL autoclave containing 0.3 g of thiourea and 30 mL of ethanol and deionized water mixed solution (volume ratio = 1 : 1). The autoclave was heated at 100 °C for 12 h to convert NiCo-precursors to $Ni_{1.4}Co_{1.6}S_4$. As a result, the crude $Ni_{1.4}Co_{1.6}S_4$/NGF was obtained, which was washed with deionized water and lyophilized for 24 h, followed by being calcined under Ar_2 at 400 °C for 3 h to get the final product $Ni_{1.4}Co_{1.6}S_4$/NGF. The mass loading of $Ni_{1.4}Co_{1.6}S_4$ on the $Ni_{1.4}Co_{1.6}S_4$/NGF composite electrode was weighted to be ~2 mg cm^{-2}. It should be noted that slight surface area error of NGF from one substrate to another exits.

2.4 Characterizations

The microstructural morphologies of the samples were obtained by scanning electron microscopy (SEM, Supra55, Zeiss, Germany) and transmission electron microscopy (TEM, Tecnai G2F20S-TWIN). The crystal structures were characterized using X-ray diffraction (XRD, D/max-UItimaIII, Rigaku, Japan) equipped with Cu Kα radiation (λ = 0.15418 nm) at a 5° min^{-1} scanning rate (2θ, 580°). The elemental composition was confirmed by X-ray photoelectron spectroscopy (XPS, ESCALAB 250). The graphitic structure was evaluated by Raman spectroscopy (inVia + Reflex, Renishaw). The specific surface area was measured by nitrogen adsorption/desorption isotherms (3Flex Surface Characterization Analyzer, USA).

The electrochemical performance of various composites was measured by an electrochemical working station (CHI 660D, CH Instruments, China) using a three-electrode testing mode and 6 M KOH aqueous solution as electrolyte. The as-prepared NGF and $Ni_{1.4}Co_{1.6}S_4$/NGF were directly tested in company with Pt foil and Hg/HgO electrode as the counter electrode and reference electrode respectively. The control $Ni_{1.4}Co_{1.6}S_4$ electrode was prepared through mixing 85 wt% of the $Ni_{1.4}Co_{1.6}S_4$ particles, 10 wt% of carbon black and 5 wt% of polyvinylidene fluoride (PVDF) in *N*-methylpyrrolidone, followed by being loaded on a Ni foam current collector (1 cm × 1 cm), dried at 80 °C overnight and compressed at 10 MPa for 1 min prior to use.

The C_{sc} was calculated from chronopotentiometry (CP) curves according to the following equation:

$$C_{sc} = \frac{I \times \Delta t}{m \times \Delta V}$$

where I (A) is the discharge current, Δt (s) is the discharge time, m (g) is the mass of the active material on the electrode, and ΔV (V) is the potential window in one sweep segment.

In the two-electrode system, a coin-type cell (CR2032) was employed to prepare the asymmetric supercapacitor, in which the $Ni_{1.4}Co_{1.6}S_4$/NGF and activated carbon were served as the positive and negative electrode, respectively. The separator used was a porous polypropylene membrane. The mass loading of $Ni_{1.4}Co_{1.6}S_4$ in the ASC was 2.3 mg cm^{-2}. Two pieces of asymmetric supercapacitors were connected in series to power a LED bulb at room temperature.

3. Results and discussion

Our approach to fabricate the porous $Ni_{1.4}Co_{1.6}S_4$ nanosheets hydrothermally grown on NGF substrate as pseudocapacitor electrodes are shown in Scheme 1. Firstly, the GF was coated with a layer of PANI through ultrasonic polymerization followed by a pyrolysis process at high temperature to obtain the N-doped GF. Secondly, a two-step hydrothermal process was conducted to grow $Ni_{1.4}Co_{1.6}S_4$ on the NGF, which includes prior incorporation of Ni, Co ions under alkaline conditions and subsequent S^{2-}-induced corrosion process. During the

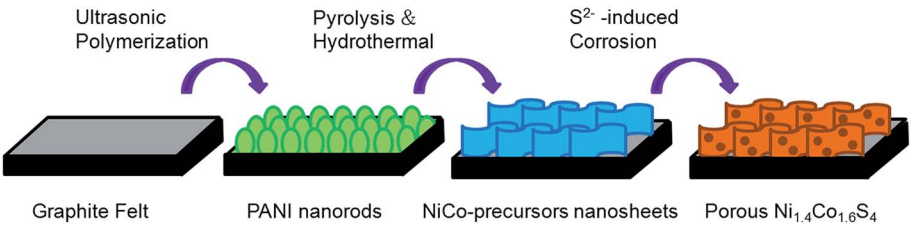

Scheme 1 Synthesis route for the $Ni_{1.4}Co_{1.6}S_4$/NGF.

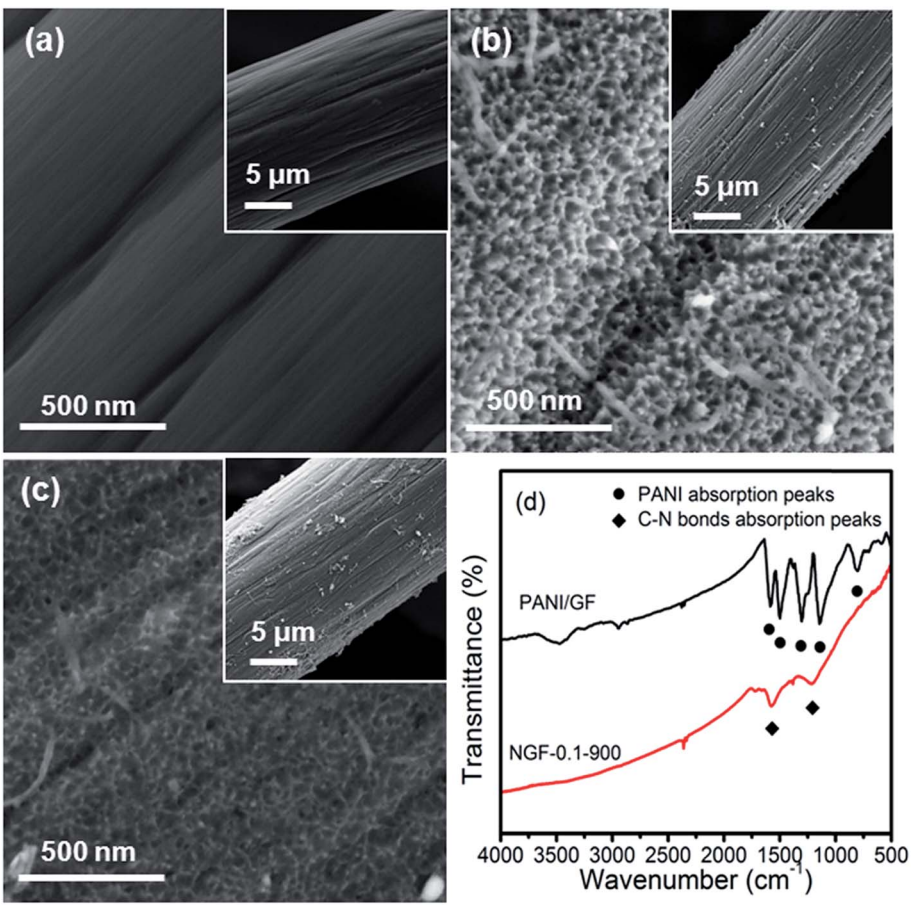

Fig. 1 Low and high resolution SEM images of the (a) pure GF, (b) PANI/GF, (c) NGF-0.1-900; FT-IR spectra of the (d) PANI/GF and NGF-0.1-900.

corrosion process, thiourea served as the sulfur source to convert smooth NiCo-precursors nanosheets into porous $Ni_{1.4}Co_{1.6}S_4$ nanosheets. The direct growth of porous $Ni_{1.4}Co_{1.6}S_4$ nanosheets on the NGF, instead of being loaded on Ni foam with polymer binder and conductive additives, is expected to achieve a uniform distribution and good adhesion of $Ni_{1.4}Co_{1.6}S_4$, which are desirable properties for high performance pseudocapacitor electrodes.

The Raman spectroscopy and cyclic voltammetry (CV) were measured firstly to evaluate the structure and the performance of the NGF electrodes polymerized with different aniline concentration. In Raman spectra (Fig. S1†), all of the samples exhibit two similar peaks, corresponding to D band and G band of graphite. The intense D band corresponds to the quantity of defects and structural disorder.[25] The integrated area ratio of D and G bands (I_D/I_G) of NGF-0.1-900 is 1.37, the highest among all the samples. This result implies the highest degree of defects and disorder in the NGF-0.1-900 on account of N-doping. To measure the electrochemical performance, CV tests (Fig. S2†) were performed on the NGF electrodes at 5 mV s^{-1} in 6 M KOH electrolyte within a voltage window of 0.0–0.8 V. The proximately rectangular-shaped CV curves suggest the existence of double-layer capacitance of the NGF electrodes.[26] NGF-0.1-900 possesses the largest enclosed area in the CV curve, suggesting the highest specific capacitance among all the NGF samples, in good keeping with the Raman result.

The morphology of the GF, PANI/GF and NGF-0.1-900 was characterized by SEM, as shown in Fig. 1. It's clear in Fig. 1(a) that the GF fiber with a diameter about 15 μm contains some shallow trenches on the smooth surface, which provide expanded surface area and lower interface energy to facilitate the nucleation of PANI.[27] After ultrasonic polymerization of aniline monomers, PANI nanorods are retained and vertically grown on the GF surface, as shown in Fig. 1(b). The origin of this vertical morphology is either due to the strong interaction between conjugated structure and π bond[27] or the electrostatic and hydrogen bonding interactions between positive functional groups of aniline and negative ones of the GF.[28] Ultrasonic irradiation contributes to the good solubility of aniline monomer and oxidant through cavitation and vibration effect,[29–31] which enhance the reaction rate and suppress secondary growth to prevent PANI from agglomeration.[32] In Fig. 1(c), the nanorods are almost disappeared. Such a structural alteration implies that PANI layer had been decomposed in this pyrolysis process. In Fig. 1(d), the IR absorption peaks of C–N bonds (around 1570 cm^{-1} and 1210 cm^{-1}) appeared after pyrolysis process, while the absorption peaks of PANI disappeared (around 1635 cm^{-1}, 1466 cm^{-1}, 1292 cm^{-1}, 1088 cm^{-1} and 791 cm^{-1}).[33] The IR results also demonstrate the decomposition of PANI and the incorporation of nitrogen atoms into GF.

Temperature is an important factor to influence the N content and surface area of NGFs. The element compositions of the NGFs pyrolyzed at three different temperatures (800, 900,

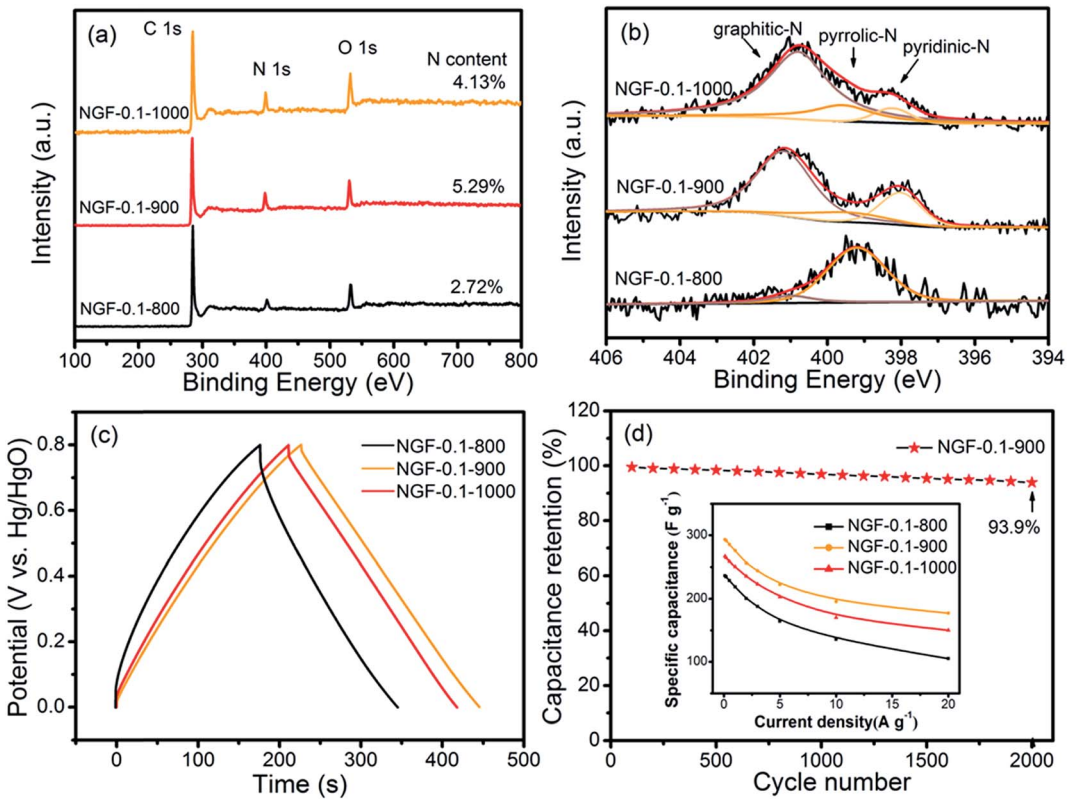

Fig. 2 (a) XPS survey spectra, (b) N 1s deconvoluted spectra, (c) charge/discharge curves of the NGF-0.1-800, NGF-0.1-900 and NGF-0.1-1000 at the current density of 1 A g^{-1}, (d) cycling performance of the NGF-0.1-900 at a current density of 10 A g^{-1}; the inset figure shows the rate capability of the NGF-0.1-800, NGF-0.1-900 and NGF-0.1-1000.

1000 °C) were characterized by XPS, as shown in Fig. 2. The XPS survey spectra (Fig. 2(a)) of the NGFs show C, N, O signals for all samples, suggesting the successful incorporation of N atoms. The N contents for the NGF-0.1-800, NGF-0.1-900 and NGF-0.1-1000 are derived to be 2.72%, 5.29%, and 4.13%, respectively. In the deconvoluted N 1s spectra (Fig. 2(b)), three peaks appointed to pyridinic-N (398.4 eV), pyrrolic-N (399.7 eV) and graphitic-N (401.2 eV) can be found.[34] The distributions of these three types of N are shown in Table S1.† The results showed that pyrrolic-N dominated at 800 °C but evolved to form graphitic and pyridinic N when the temperature was increased to 900 °C. The largest content of pyridinic-N was obtained at 900 °C, which gradually went down when the temperature rose to 1000 °C. The nitrogen adsorption–desorption isotherms of the samples (Fig. S3†) and the derived specific surface area, pore volume and pore diameter (Table S2†) showed that the samples were mesoporous and the Brunauer–Emmett–Teller (BET) specific surface area decreased from 56.78 $m^2 g^{-1}$ to 41.42 $m^2 g^{-1}$ as the pyrolysis temperature increased from 800 to 1000 °C.

The electrochemical performance of the NGFs was characterized to screen a best substrate for further study. As shown in Fig. 2(c), the NGF-0.1-900 exhibits the longest charge/discharge time at the current density of 1 A g^{-1}. The specific capacitance of NGF-0.1-900 is calculated to be 276 F g^{-1}, much higher than the 219 F g^{-1} of NGF-0.1-800 and the 250 F g^{-1} of NGF-0.1-1000 under the same testing condition. This result implies that 900 °C is an optimal pyrolysis temperature for NGFs, and NGF-0.1-900 is an appropriate substrate for further study. These

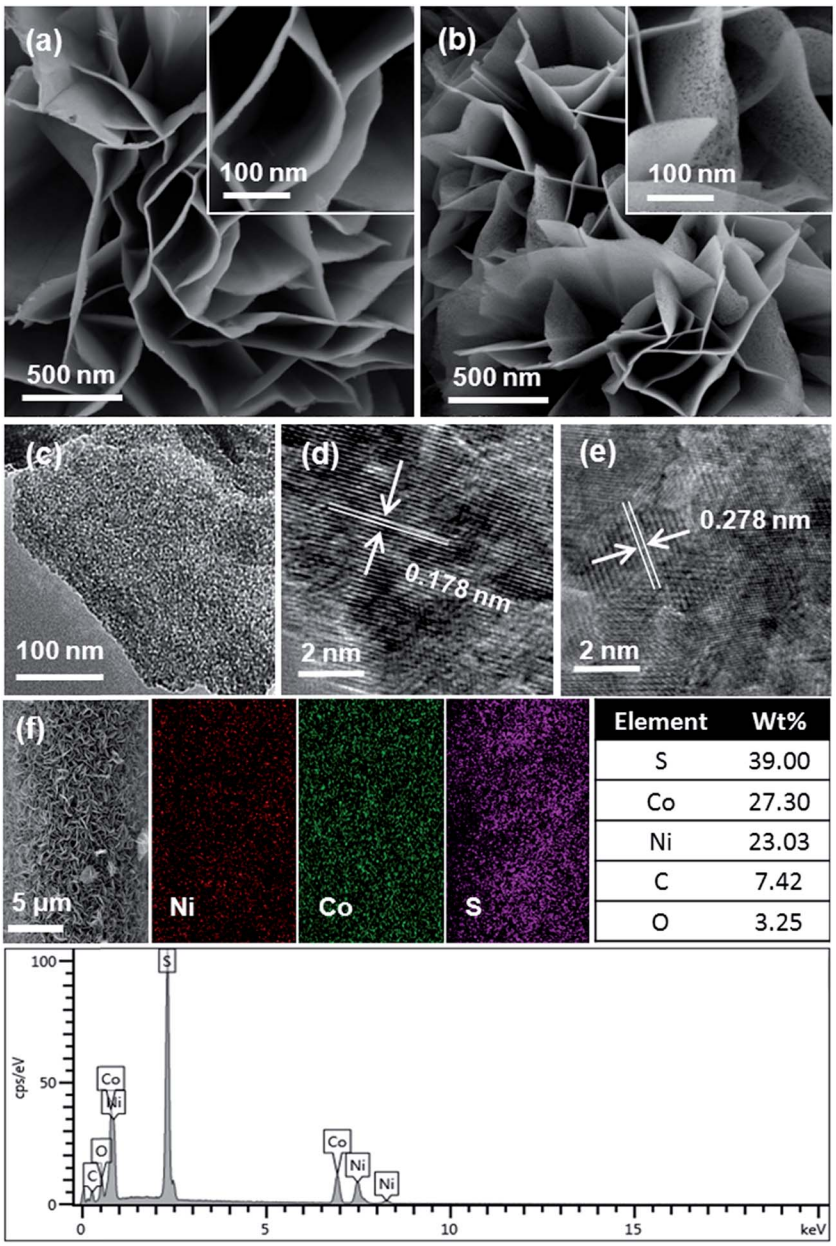

Fig. 3 (a) Low and high resolution SEM images of NiCo-precursors nanosheets grown on the NGF-1-900. (b) SEM images, (c) TEM image, (d and e) HRTEM images, (f) EDS elemental mapping images and spectrum of the $Ni_{1.4}Co_{1.6}S_4$/NGF.

conclusions are also confirmed by the cycling and rate capability tests, as shown in Fig. 2(d), where it can be found that the NGF-0.1-900 presents a good cycling stability with only 6% decrease of specific capacitance after 2000 cycles at a current density of 10 A g^{-1}. For all the tested current rates, NGF-0.1-900 shows the highest specific capacitance than the others. Since the BET specific surface area of NGF-0.1-900 is not the largest among the above three samples, it seems that the content of pyridinic-N is the dominating factor leading to the best performance of NGF-0.1-900.

Substituting N atom into graphite felt will definitely reduce the HOMO–LUMO gap, which makes it energetically favorable for electrons to be excited from valence band to conduction band.[35] Moreover, richness of disorder (different forms of carbon–nitrogen bond) and abundance of nitrogen-associated functional groups accelerate charge transfer at the material interface.[36,37] In addition, with an unpaired electron, nitrogen possesses a strong electron-withdrawing ability to lead to positive charge density of carbon atoms adjacent, thus providing active sites for redox reaction.[38,39] These effects will be intensified by the pyridinic-N that possesses stronger electron withdrawing ability than the other types of nitrogen bonds.[14] These may be the reasons why NGF-0.1-900 outperforms the other samples.

To coat NGF-0.1-900 with redox-active sulfides, an oxidation process to introduce structural defects was performed, which was monitored by the FT-IR spectrum (Fig. S4†). After that, a two-step hydrothermal method was adopted to synthesize

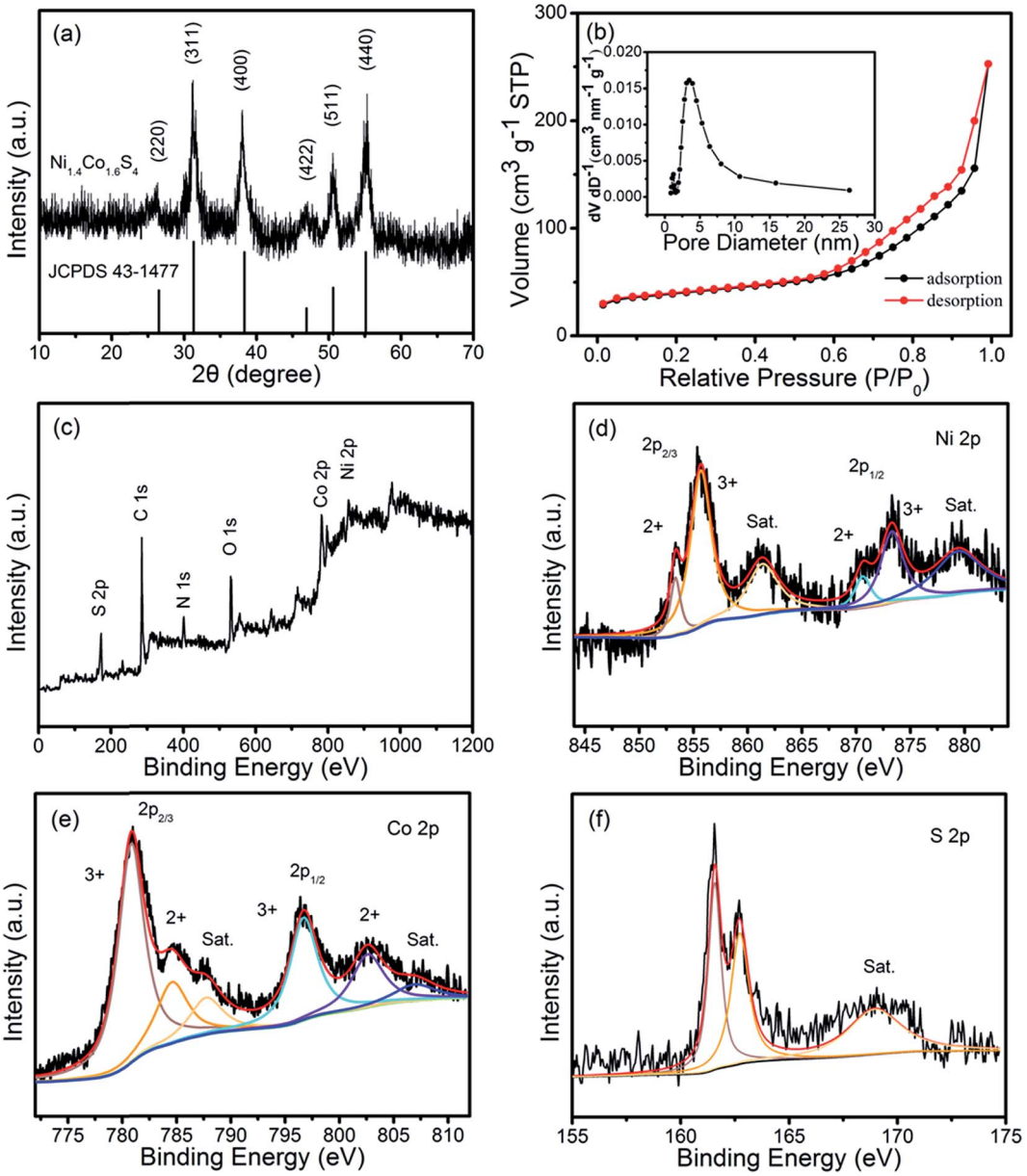

Fig. 4 (a) XRD pattern of the $Ni_{1.4}Co_{1.6}S_4$ scratched from the $Ni_{1.4}Co_{1.6}S_4$/NGF; (b) nitrogen adsorption–desorption isotherm of the $Ni_{1.4}Co_{1.6}S_4$/NGF; (c) XPS survey spectrum; (d) XPS Ni 2p spectrum; (e) XPS Co 2p spectrum; (f) XPS S 2p spectrum.

$Ni_{1.4}Co_{1.6}S_4$/NGF, involving prior *in situ* growth of NiCo-precursors ($Ni_{2/3}Co_{4/3}(CO_3)(OH)_2$)[40] on the NGF substrate and subsequent S^{2-}-induced corrosion reaction. Fig. 3(a) shows the SEM image of NiCo-precursors nanosheets grown on NGF surface. Higher magnification image in Fig. 3(a) further reveals that the nanosheets have smooth surface with a thickness of a few nanometers. During the sulfurization process, the opening structure of the NiCo-precursors provides sufficient space and surface for the diffusion of S^{2-} ions. An appropriate amount of S^{2-} ions react with NiCo-precursors that served as a sacrificial template to form porous $Ni_{1.4}Co_{1.6}S_4$ (Fig. 3(b)). Compared with the NiCo-precursors nanosheets, the $Ni_{1.4}Co_{1.6}S_4$ preserved the overall morphology, except the smaller thickness as well as distinct pores that distributed throughout the surface.

The TEM image (Fig. 3(c)) of the $Ni_{1.4}Co_{1.6}S_4$ shows numerous porous structures with a diameter of about 2 nm uniformly formed on the surface, which may be resulted from the continuous ion exchange between S^{2-} and CO_3^{2-}/OH^- of the NiCo-precursors.[40] The lattice spacing of 0.178 nm and 0.278 nm in HRTEM images (Fig. 3(d) and (e)) correspond to the (511) and (311) planes (0.18 nm and 0.28 nm) of the $NiCo_2S_4$.[40] Energy-dispersive X-ray spectroscopy (EDS) (Fig. 3(f)) of the $Ni_{1.4}Co_{1.6}S_4$/NGF exhibits well-distributed Ni, Co and S atoms throughout the nanostructure. The molar ratio of Ni : Co : S is about 1.4 : 1.6 : 4, in consistent with the molar ratio of the starting materials. All these results suggest the successful synthesis of $Ni_{1.4}Co_{1.6}S_4$ on NGF surface.

The crystal structure of the $Ni_{1.4}Co_{1.6}S_4$ scraped from the $Ni_{1.4}Co_{1.6}S_4$/NGF was characterized by X-ray diffraction, as shown in Fig. 4(a). The overall diffraction peaks of highly-crystallized $Ni_{1.4}Co_{1.6}S_4$ can be indexed to the cubic $NiCo_2S_4$ phase (JCPDS card no. 43-1477), but all characteristic peaks migrate to the low angle direction, owing to the decrease of Co element that has the bigger lattice parameter than Ni. In the nitrogen adsorption–desorption isotherms (Fig. 4(b)), a hysteresis loop at the P/P_0 range of 0.6–1.0 can be seen, indicating the mesoporous feature of the $Ni_{1.4}Co_{1.6}S_4$/NGF. The BET specific surface area is calculated to be 141.5 $m^2\ g^{-1}$, and the pore diameter from Barrett–Joyner–Halenda (BJH) analysis is about 4.0 nm, which is favorable for ion diffusion.

Element compositions and atomic valence states of the $Ni_{1.4}Co_{1.6}S_4$/NGF were evaluated by XPS measurements. The presence of Ni, Co, S, N, and C atoms can be clearly seen from Fig. 4(c). In Fig. 4(d), the Ni 2p core-level spectrum shows two spin–orbit doublets and two shake-up satellites, indicating that the atoms of Ni are in the divalent (853.6 eV, 871.6 eV) and trivalent states (855.4 eV, 873.3 eV).[41] Similarly, two spin–orbit doublets and shake-up satellites also show up in the Co 2p spectrum (Fig. 4(e)), characteristic of Co^{2+} and Co^{3+}. As shown in the Fig. 4(f), the S 2p region can be fitted with two main peaks (161.6 eV, 162.7 eV) and one shake-up satellite (169.0 eV). The peak at 161.6 eV is ascribed to S^{2-}, and the peak at 162.7 eV is ascribed to the metal–sulfur bonds forming at the surface.[42,43] These results demonstrate that the $Ni_{1.4}Co_{1.6}S_4$/NGF contains

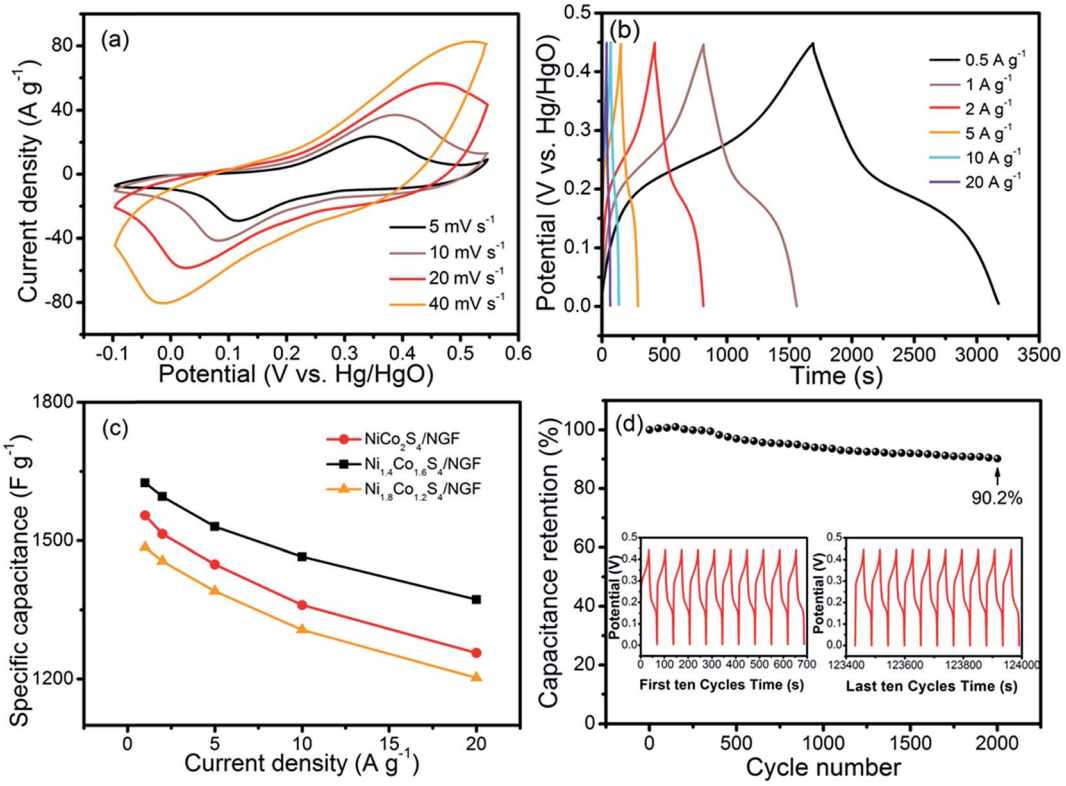

Fig. 5 (a) CV curves of the $Ni_{1.4}Co_{1.6}S_4$/NGF electrode at different scan rates. (b) CP curves of the $Ni_{1.4}Co_{1.6}S_4$/NGF electrode at different current densities. (c) Rate capability of the $NiCo_2S_4$/NGF, $Ni_{1.4}Co_{1.6}S_4$/NGF and $Ni_{1.8}Co_{1.2}S_4$/NGF electrodes. (d) Cycling performance of the $Ni_{1.4}Co_{1.6}S_4$/NGF electrode at a current density of 20 A g^{-1}.

Co^{2+}, Co^{3+}, Ni^{2+}, Ni^{3+} and S^{2-}, in good agreement with previous reports about nickel cobalt sulfides.[23,42–45]

Cyclic voltammetry and charge/discharge measurements were carried out to evaluate the electrochemical performance of the $Ni_{1.4}Co_{1.6}S_4$/NGF electrode. In Fig. 5(a), a pair of redox peaks corresponding to the reversible reactions of Ni^{2+}/Ni^{3+}, Co^{2+}/Co^{3+} and Co^{3+}/Co^{4+} (ref. 46 and 47) can be easily observed. As the scan rate increases, the anodic and cathodic peaks shift to more positive and negative potentials, respectively. When the scan rate is increased to 40 mV s^{-1}, the pair of redox peaks is still visible, suggesting that the $Ni_{1.4}Co_{1.6}S_4$/NGF can afford fast reversible faradaic reactions for rapid charge/discharge processes.[23,48] Chronopotentiometry (CP) curves of the $Ni_{1.4}Co_{1.6}S_4$/NGF electrode at various current densities ranging from 0.5 to 20 A g^{-1} are illustrated in Fig. 5(b). Consistent with the CV results, all of the curves are approximately symmetric and have plateaus characteristic of faradaic behavior during charge/discharge process.[3,49] The specific capacitance derived from the CP curves for the $Ni_{1.4}Co_{1.6}S_4$/NGF electrode at the current density of 0.5 A g^{-1} is 1634 F g^{-1}, and it remains 1372 F g^{-1} at the current density of 20 A g^{-1}, suggesting a remarkable rate capability of the electrode.

The influence of Ni/Co ratio on the electrochemical performance of NGF based electrode was also investigated. As shown in Fig. 5(c), the $NiCo_2S_4$/NGF and $Ni_{1.8}Co_{1.2}S_4$/NGF electrodes exhibit smaller specific capacitance than the $Ni_{1.4}Co_{1.6}S_4$/NGF electrode at all the tested current rates. This result is in consistent with the CV (Fig. S5†) and CP test (Fig. S6†). Therefore, carefully selection of Ni/Co ratio is important for the electrode development. The promising electrochemical

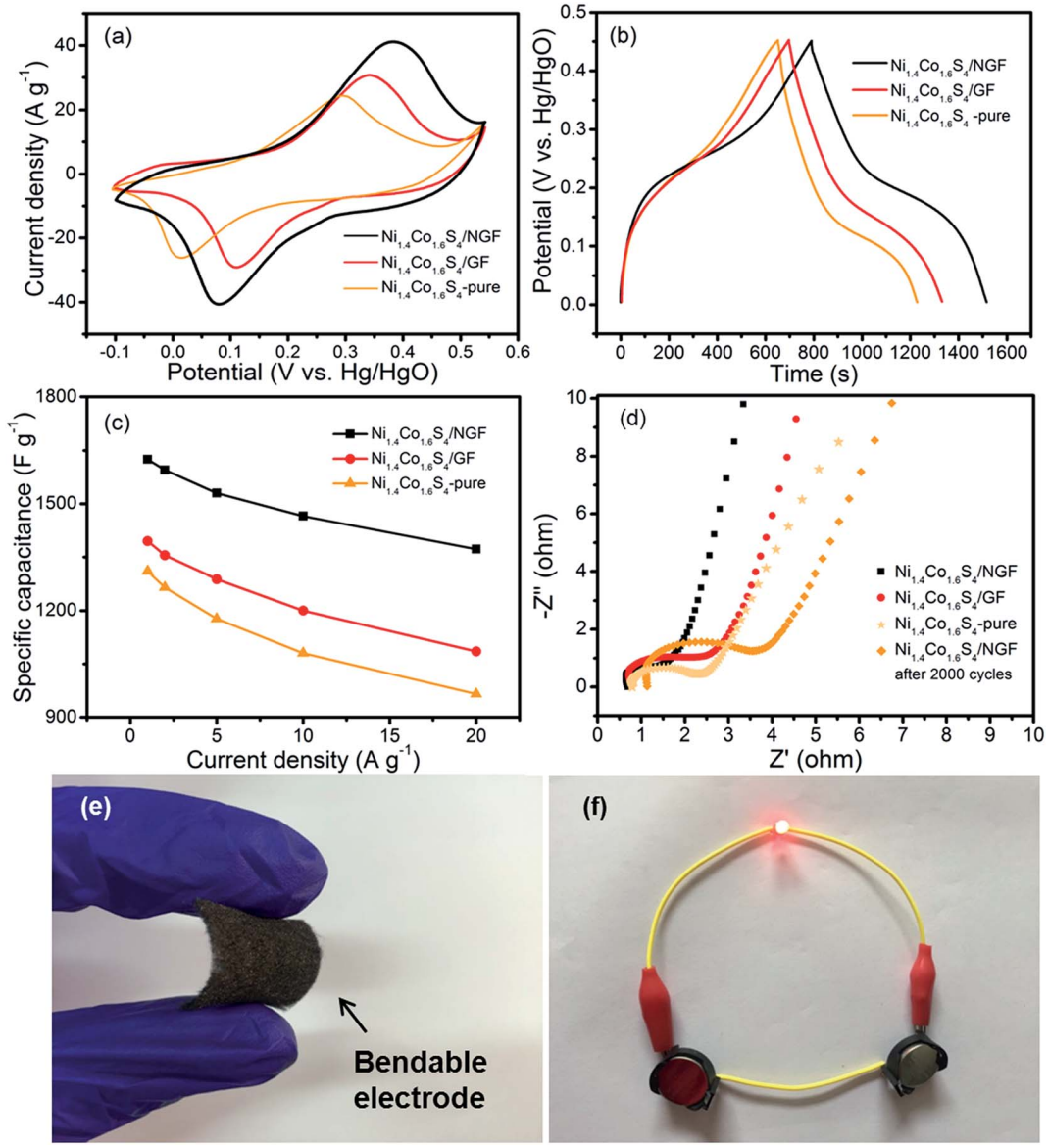

Fig. 6 (a) CV curves, (b) CP curves, (c) rate capacity, and (d) Nyquist plots of the $Ni_{1.4}Co_{1.6}S_4$/NGF, $Ni_{1.4}Co_{1.6}S_4$/GF and pure $Ni_{1.4}Co_{1.6}S_4$ electrodes; (e) a digital photo of the bendable $Ni_{1.4}Co_{1.6}S_4$/NGF electrode. (f) Experimental demonstration of the $Ni_{1.4}Co_{1.6}S_4$/NGF based device lighting up a LED bulb.

performance of the $Ni_{1.4}Co_{1.6}S_4$/NGF electrode was further verified by the long-term cycling tests at a current density of 20 A g^{-1}, as shown in Fig. 5(d). It can be seen that the specific capacitance increases slightly in the first 150 cycles, due to the activation of the material. After that, the value decreases gradually as the cycling proceeds, and finally retains 90.2% of the original value after 2000 cycles. The minor decay in specific capacitance is also reflected by the slight decrease of charge/discharge time after 2000 cycles. Such encouraging stability can be attributed to the strong adhesion between $Ni_{1.4}Co_{1.6}S_4$ and NGF, and the favorable $Ni_{1.4}Co_{1.6}S_4$ nanostructure that almost remains unchanged after cycling (Fig. S7†).

To prove the positive contribution of 3D NGF substrate to the electrochemical performance of the $Ni_{1.4}Co_{1.6}S_4$/NGF electrode, $Ni_{1.4}Co_{1.6}S_4$/GF and pure $Ni_{1.4}Co_{1.6}S_4$ electrodes were prepared as control. The pure $Ni_{1.4}Co_{1.6}S_4$ electrode used Ni foam as substrate, PVDF as binder, carbon black as conductive additive, following the traditional blending protocol. As it can be seen from Fig. 6(a), the $Ni_{1.4}Co_{1.6}S_4$/NGF electrode has the largest enclosed CV area compared to the other two electrodes. In Fig. 6(b), the $Ni_{1.4}Co_{1.6}S_4$/NGF electrode exhibits the longest charge/discharge time in the CP testing. Both the CV and CP results suggest that the NGF is essentially important for the promising electrochemical performance of the $Ni_{1.4}Co_{1.6}S_4$/NGF electrode. The specific capacitance of the $Ni_{1.4}Co_{1.6}S_4$/NGF electrode is the highest than those of the other electrodes at all the current rate tested, as shown in Fig. 6(c). Therefore, the NGF substrate not only contributes to the electrostatic double layer capacitance, but also supports $Ni_{1.4}Co_{1.6}S_4$ to achieve an overall electrochemical performance that cannot be realized by either GF or Ni foam substrate.

The mechanism of the beneficial effect of the NGF substrate for the overall electrochemical performance of the $Ni_{1.4}Co_{1.6}S_4$/NGF electrode was investigated by electrochemical impedance spectroscopy (EIS), as shown in Fig. 6(d). Four basic features can be derived from the Nyquist plots of the $Ni_{1.4}Co_{1.6}S_4$/NGF, $Ni_{1.4}Co_{1.6}S_4$/GF and pure $Ni_{1.4}Co_{1.6}S_4$ electrodes: (1) the R_s (equivalent series resistance, derived from the intersection of the EIS curve with *X*-axis at high frequency region) of the $Ni_{1.4}Co_{1.6}S_4$/NGF electrode is about 0.7 ohm, lower than 1.2 ohm of the pure $Ni_{1.4}Co_{1.6}S_4$; (2) the R_{ct} (charge-transfer resistance, derived from the diameter of EIS semicircle at medium-frequency region) of the $Ni_{1.4}Co_{1.6}S_4$/NGF electrode is relatively small; (3) in the low frequency range, the $Ni_{1.4}Co_{1.6}S_4$/NGF electrode holds a more vertical line, signifying the better capacitive performance and the lower Warburg resistance;[50] (4) after cycling for 2000 times, the $Ni_{1.4}Co_{1.6}S_4$/NGF electrode shows an increased semi-arc and a lower slope, implying a higher R_{ct} and lower ionic diffusion rate at the interface.[51] These results suggest that the NGF helps to decrease the electric resistance of the $Ni_{1.4}Co_{1.6}S_4$/NGF. Without NGF substrate, the $Ni_{1.4}Co_{1.6}S_4$ sheets tend to aggregate with a wide range of size distribution (Fig. S8†), leading to a large resistance for electrochemical reactions. The NGF has 3D electron conducting pathway as well as excellent polar surface with defects to afford the growth of uniformly dispersed $Ni_{1.4}Co_{1.6}S_4$ nanosheets. Therefore, the synergetic effect of the good electron conductivity and excellent surface property of the NGF may be the primary reason for the enhanced electrochemical performance of the $Ni_{1.4}Co_{1.6}S_4$/NGF electrode.

Besides the remarkable electrochemical performance, the $Ni_{1.4}Co_{1.6}S_4$/NGF electrode is a stand-alone and bendable electrode that doesn't need polymer binder, metal substrate, and conductive additives. These are key properties that have attracted the interests from both academic and industrial communities for the development of wearable electronics. A digital photo of a bended $Ni_{1.4}Co_{1.6}S_4$/NGF electrode was given in Fig. 6(c) to prove the bendable nature of such materials design. Also, two asymmetric supercapacitors based on the $Ni_{1.4}Co_{1.6}S_4$/NGF electrode and activated carbon electrode were assembled in series to light up a LED bulb, as shown in Fig. 6(f). It can be expected that the $Ni_{1.4}Co_{1.6}S_4$/NGF electrode and its analogs pave the way for the design of next-generation pseudocapacitors.

4. Conclusions

Nitrogen doped graphite felts (NGFs) were successfully prepared as substrate for the decoration of porous NiCo-sulfides redox-active nanosheets for 3D pseudocapacitor electrodes. The incorporation of nitrogen atom was realized by the pyrolysis of polyaniline formed on the surface of graphite felt. NiCo-precursors were then hydrothermally grown on the NGF, followed by S^{2-}-induced corrosion process to make the corresponding NiCo-sulfides for the stand-alone and bendable composite electrode. It was found that 0.1 M of aniline concentration and 900 °C of pyrolysis temperature were the best conditions for making NGFs. The composition of NiCo-sulfides was optimized based on the electrochemical characterizations of the resultant electrodes. The $Ni_{1.4}Co_{1.6}S_4$/NGF electrode turned out to be the best electrode in terms of specific capacitance (1625 F g^{-1} at a current density of 1 A g^{-1}) and cycling stability (90.2% of capacitance retention after 2000 cycles at a current density of 20 A g^{-1}). These remarkable electrochemical properties were attributed to the desirable $Ni_{1.4}Co_{1.6}S_4$ nanostructure and the synergistic effect of the good electron conductivity and excellent surface property of the NGF substrate.

Acknowledgements

This work was supported by the National Natural Science Foundation of China (Grant Number 51503038), Scientific and Technological Innovation Project of Fujian Province (Grant Number 2012H6008), and Scientific and Technological Innovation Project of Fuzhou City (Grant Number 2013-G-92).

References

1 A. M. Abioye and F. N. Ani, *Renewable Sustainable Energy Rev.*, 2015, **52**, 1282–1293.
2 R. Farma, M. Deraman, A. Awitdrus, I. A. Talib, E. Taer, N. H. Basri, J. G. Manjunatha, M. M. Ishak, B. N. M. Dollah and S. A. Hashmi, *Bioresour. Technol.*, 2013, **132**, 254–261.

3 Y. F. Zhang, M. Z. Ma, J. Yang, C. C. Sun, H. Q. Su, W. Huang and X. Dong, *Nanoscale*, 2014, **6**, 9824–9830.
4 Y. Ma, W. Chen, P. Zhang, F. Teng, J. Zhou, X. Pan and E. Xie, *RSC Adv.*, 2014, **4**, 47609–47614.
5 A. S. Arico, P. Bruce, B. Scrosati, J. M. Taracson and W. V. Schalkwijk, *Nat. Mater.*, 2005, **4**, 366–377.
6 Z. Tang, C. H. Tang and H. Gong, *Adv. Funct. Mater.*, 2012, **22**, 1272–1278.
7 Y. G. Wang, H. Q. Li and Y. Y. Xia, *Adv. Mater.*, 2006, **18**, 2619–2623.
8 C. P. Ewels and M. Glerup, *J. Nanosci. Nanotechnol.*, 2005, **5**, 1345–1363.
9 L. Yan, H. Yu, S. Qian, P. Li, X. Lin, N. Long, R. Zhang, M. Shui and J. Shu, *Electrochim. Acta*, 2016, **213**, 217–224.
10 Y. J. Lee, W. P. Hai, S. Park and I. K. Song, *Curr. Appl. Phys.*, 2012, **12**, 233–237.
11 B. L. Ouay, T. Coradin and C. Laberty-Robert, *J. Phys. Chem. C*, 2013, **117**, 15918–15923.
12 M. Srivastavaa, M. E. Uddina, J. Singhb, N. H. Kima and J. H. Lee, *J. Alloys Compd.*, 2014, **590**, 266–276.
13 Z. He, J. Shi, Z. He and S. Liu, *Int. J. Energy Res.*, 2015, **39**, 709–716.
14 H. M. Jeong, J. W. Lee, W. H. Shin, Y. J. Choi, H. J. Shin, J. K. Kang and J. W. Choi, *Nano Lett.*, 2011, **11**, 2472–2477.
15 L. Yu, B. Yang, Q. Liu, J. Y. Liu, X. Wang, D. L. Song, J. Wang and X. Y. Jing, *J. Electroanal. Chem.*, 2015, **739**, 156–163.
16 J. C. Xing, Y. L. Zhu, M. Y. Li and Q. J. Jiao, *Electrochim. Acta*, 2014, **149**, 285–292.
17 S. Peng, L. Li, C. Li, H. Tan, R. Cai, H. Yu, S. Mhaisalkar, M. Srinivasan, S. Ramakrishna and Q. Yan, *Chem. Commun.*, 2013, **86**, 10178–10180.
18 J. G. Wang, R. Zhou, D. Jin, K. Xie and B. Wei, *Energy Storage Materials*, 2016, **2**, 1–7.
19 H. C. Chen, J. J. Jiang, L. Zhang, H. Z. Wan, T. Qi and D. D. Xia, *Nanoscale*, 2013, **5**, 8879–8883.
20 J. W. Xiao, X. W. Zeng, W. Chen, F. Xiao and S. Wang, *Chem. Commun.*, 2013, **49**, 11734–11736.
21 R. Ding, M. Zhang, Y. Yao and H. Gao, *J. Colloid Interface Sci.*, 2016, **467**, 140–147.
22 T. Zhu, G. Zhang, T. Hu, Z. He, Y. Lu, G. Wang, H. Guo, J. Luo, C. Lin and Y. Chen, *J. Mater. Sci.*, 2016, **51**, 1903–1913.
23 M. Sun, J. Tie, G. Cheng, T. Lin, S. Peng, F. Deng, F. Ye and L. Yu, *J. Mater. Chem. A*, 2015, **3**, 1730–1736.
24 X. B. Liu, P. B. Shang, Y. B. Zhang, X. L. Wang, Z. M. Fan, B. X. Wang and Y. Y. Zheng, *J. Mater. Chem. A*, 2014, **2**, 15273–15278.
25 M. Sevilla and A. B. Fuertes, *ACS Nano*, 2014, **8**, 5069–5078.
26 Z. Ma, X. Huang, S. Dou, J. Wu and S. Wang, *J. Phys. Chem. C*, 2014, **118**, 17231–17239.
27 W. Li, Y. Ye, X. Lu, Z. Wen, Z. Li, H. Hou and Y. Song, *Sci. Rep.*, 2013, **3**, 1524–1528.
28 J. J. Xu, K. Wang, S. Z. Zu, B. H. Han and Z. Wei, *ACS Nano*, 2010, **4**, 5019–5026.
29 K. S. Suslick and G. J. Price, *Annu. Rev. Mater. Res.*, 1999, **29**, 295–326.
30 M. Atobe, A. N. Chowdhury, T. Fuchigami and T. Nonaka, *Ultrason. Sonochem.*, 2013, **10**, 77–80.
31 H. Xia and Q. Wang, *J. Nanopart. Res.*, 2001, **3**, 399–409.
32 X. Jing, Y. Wang, D. Wu and J. Qiang, *Ultrason. Sonochem.*, 2007, **14**, 75–80.
33 D. Ghosh, S. Giri, A. Mandal and C. K. Das, *Appl. Surf. Sci.*, 2013, **276**, 120–128.
34 X. M. Zhang, Y. Q. Jiao, L. Sun, L. Wang, A. P. Wu, H. J. Yan, M. C. Meng, C. G. Tian, B. J. Jiang and H. G. Fu, *Nanoscale*, 2016, **8**, 2418–2427.
35 L. Zhang and Z. Xia, *J. Phys. Chem.*, 2011, **115**, 11170–11176.
36 Y. Nagai, T. Hirabayashi, K. Dohmae, N. Takagi, T. Minami, H. Shinjoh and S. Matsumoto, *J. Catal.*, 2006, **242**, 103–109.
37 G. Wu and B. Q. Xu, *J. Power Sources*, 2007, **174**, 148–158.
38 L. T. Qu, Y. Liu, J. B. Baek and L. M. Dai, *ACS Nano*, 2010, **4**, 1321–1326.
39 D. S. Yu, Q. Zhang and L. M. Dai, *J. Am. Chem. Soc.*, 2010, **132**, 15127–15129.
40 X. Wu, S. Li, B. Wang, J. Liu and M. Yu, *Phys. Chem. Chem. Phys.*, 2016, **18**, 4505–4512.
41 D. Cai, D. Wang, C. Wang, B. Liu, L. Wang, Y. Liu, Q. Li and T. Wang, *Electrochim. Acta*, 2015, **151**, 35–41.
42 H. Chen, J. Jiang, L. Zhang, D. Xia, Y. Zhao, D. Guo, T. Qi and H. Wan, *J. Power Sources*, 2014, **254**, 249–257.
43 Y. Liu, J. Zhang, S. Wang, K. Wang, Z. Chen and Q. Xu, *New J. Chem.*, 2014, **38**, 4045–4048.
44 Q. Wang, L. Jiao, H. Du, Y. Si, Y. Wang and H. Yuan, *J. Mater. Chem.*, 2012, **22**, 21387–21391.
45 Y. Zhang, C. Sun, H. Su, W. Huang and X. Dong, *Nanoscale*, 2015, **7**, 3155–3163.
46 H. Wan, X. Ji, J. Jiang, J. Yu, L. Miao, L. Zhang, S. Bie, H. Chen and Y. Ruan, *J. Power Sources*, 2013, **243**, 396–402.
47 L. Mei, T. Yang, C. Xu, M. Zhang, L. Chen, Q. Li and T. Wang, *Nano Energy*, 2014, **3**, 36–45.
48 W. B. Fu, C. H. Zhao, W. H. Han, Y. Liu, H. Zhao, Y. F. Ma and E. Q. Xie, *J. Mater. Chem. A*, 2015, **3**, 10492–10497.
49 Q. Wang, Y. Zhu, J. Xue, X. Zhao, Z. Guo and C. Wang, *ACS Appl. Mater. Interfaces*, 2016, **8**, 17226–17232.
50 L. Wang, Z. H. Dong, Z. G. Wang, F. X. Zhang and J. Jin, *Adv. Funct. Mater.*, 2013, **23**, 2758–2764.
51 J. Pu, F. L. Cui, S. B. Chu, T. T. Wang, E. H. Sheng and Z. H. Wang, *ACS Sustainable Chem. Eng.*, 2014, **2**, 809–815.